EUV burst, particle heating and whistler wave emission in fast magnetic reconnection induced by kink-driven Rayleigh-Taylor instability

Kil-Byoung Chai, Xiang Zhai, Paul M. Bellan

Applied Physics and Materials Science,

Caltech, Pasadena, CA 91125, USA

Abstract

A spatially localized energetic EUV burst is imaged at the presumed position of fast magnetic reconnection in a plasma jet produced by a coaxial helicity injection source; this EUV burst indicates strong localized electron heating. A circularly polarized high frequency magnetic field perturbation is simultaneously observed at some distance from the reconnection region indicating that the reconnection emits whistler waves and that Hall dynamics likely governs the reconnection. Spectroscopic measurement shows simultaneous fast ion heating. The electron heating is consistent with Ohmic dissipation while the ion heating is consistent with ion trajectories becoming stochastic.

I.   INTRODUCTION

Magnetic reconnection, the localized restructuring of a plasma's magnetic topology via a conversion of magnetic energy into particle energy, is critical to the dynamic evolution of the magnetosphere [1, 2], the solar corona [3], and fusion plasmas [4]. Furthermore, magnetic reconnection enables Taylor relaxation [5], the mechanism by which plasmas self-organize into spheromak [6] or reversed field pinch (RFP) configurations [7, 8].

Magnetic reconnection involves extreme magnetic non-uniformity and was long considered to be governed by a resistive magnetohydrodynamics (MHD) differential equation [9, 10] for the out-of-plane vector potential component A_z. Because this equation predicts reconnection far slower than observed [4, 11] much effort has gone into developing models predicting faster reconnection and this effort has culminated in the general agreement that fast reconnection results from Hall and finite m_e terms missing from MHD.

This fast reconnection is dynamic, i.e., not diffusive as in resistive MHD, and results from a pair of differential equations where A_z and the out-of-plane magnetic field component B_z drive each other [12–16]. In a uniform magnetic field these coupled equations simplify to describe whistler waves but in the highly non-uniform magnetic field geometry characterizing reconnection this simplification is not possible [15]. Nevertheless, whistler waves are often observed in fast reconnection contexts [1, 17–20] and the relation between reconnection and whistler waves is much debated. For example, applying results from a 2-D particle-in-cell (PIC) code, Drake et al. [14] suggested that whistler waves facilitate collisionless magnetic reconnection whereas, using a similar code, Fujimoto et al. [15] claimed instead that a reconnection-induced temperature anisotropy outside the reconnection region generates observed whistler waves. Attico et al. [21] and Bellan [16] showed that 2-D Hall reconnection is not a wave but rather a purely growing instability with growth rate of order of the whistler frequency.

The means by which reconnection converts magnetic field energy into particle energy is also controversial. On observing 2-D localized electron heating and anomalous ion heating in the Magnetic Reconnection Experiment (MRX), Yoo et al. [22] proposed that ions are first ballistically accelerated and then collisionally thermalized in the reconnection exhaust. However, on observing electron and ion heating in a merging experiment Ono et al. [23] argued that electrons are Ohmically heated whereas ions are heated by shock or viscous

2

damping in the reconnection exhaust [23].

We report the following sequence of experimental observations of a spontaneous 3-D Hall-mediated reconnection: (i) a current-carrying MHD-driven plasma jet self-forms [24], (ii) the jet undergoes a kink instability [25], (iii) the kink provides the environment for development of a secondary, Rayleigh-Taylor (RT) instability [26], (iv) the RT instability chokes the current channel radius to cause a fast localized reconnection [26], (v) the reconnection produces localized electron and ion heating, (vi) the reconnection also radiates broadband obliquely-propagating, right-hand circularly polarized whistler waves. These observations show that Hall physics is important even though the plasma jet is collisional, that electrons are plausibly heated by Ohmic dissipation, and that ions are plausibly heated stochastically. Because the configuration is a coaxial helicity source as often used for producing spheromaks [27], these observations provide new insights into the likely reconnection process underlying Taylor relaxation.

II.   EXPERIMENTAL SETUP AND KINK-INDUCED RT INSTABILITY

The experimental setup, detailed in Ref.[25, 26] and sketched in Fig. 1, creates a collimated MHD plasma jet flowing along the z-axis of a 1.6 m long, 1.4 m diameter vacuum chamber. The operational sequence is: (i) an external coil establishes a poloidal magnetic field linking a 20 cm diameter copper disk electrode to a co-planar 50 cm diameter copper annulus electrode, (ii) fast gas valves puff Ar gas through 8 holes on each of the disk and annulus, (iii) 5 kV from a 120 μF capacitor bank applied across the disk-annulus gap breaks down the gas cloud and drives current along 8 arched plasma-filled flux tubes linking disk holes to annulus holes, (iv) the inner segments of these arched flux tubes merge to form a collimated jet which proceeds to lengthen, (v) a pulse forming network sustains the 50-60 kA jet current for $\sim$ 50 μs as the jet lengthens.

A double-branch fiber bundle routes two separate images to a DRS Imacon 200 high-speed movie camera. As seen in Fig. 1, the two branches are respectively coupled to a lens that captures end-on images of plasma in visible light and to a lens that captures light from an end-on EUV imaging system [28]. The high-speed camera is also used to photograph the plasma in visible light from the side. Time- and space-resolved spectroscopic information is obtained using a vertically-aligned 12-channel optical fiber array [29] that views the

FIG. 1: Sketch of experimental setup and diagnostic layout.

jet through a vacuum chamber side window at an axial location where the RT instability occurs; assuming local thermodynamic equilibrium (LTE) spectroscopic line ratios indicate the electron temperature before kinking is T_e =2-3 eV. High-frequency vector magnetic field fluctuations are measured by a probe consisting of three orthogonal pairs of oppositely-oriented $\dot{B}$ coils placed ∼15 cm from the location of the RT instability as described in Fig. 1. Each coil is a single-turn loop of 0.047" semi-rigid coaxial cable having a small gap in its shield conductor [30]. This arrangement combined with an RF ground loop diverting technique [31] together achieve the 70 db electrostatic interference rejection necessary to observe whistler-range magnetic fluctuations.

Upon exceeding a critical length determined by the Kruskal-Shafranov kink stability criterion, the jet develops an exponentially growing kink instability [25] with $\sim 10^{10}$ m s^{-2} lateral acceleration. This acceleration provides an effective gravity pointing toward the z-axis so a magnetic RT instability occurs at the interface between the dense jet and the diffuse exterior region as shown in Figs. 2(a) and (b), captured from the side; the small finger-like structures in the figures are the RT ripples. A detailed linear perturbation analysis in cylindrical geometry shows that the lateral magnetic RT instability couples to a classic

FIG. 2: Typical time evolution of kink-induced RT instability (side view). Interframe time was 1 μs. The two typical shots shown in (a) and (b) respectively had identical experimental settings but the physical location of the RT ripples differs.

current-driven (CD) instability resulting in an intrinsically 3-D hybrid RT-CD instability [32, 33]. The RT instability is experimentally observed to choke the jet radius to the same order of magnitude as the ion skin depth c/ω_{pi}; the jet then detaches from the disk electrode indicating reconnection of previously frozen-in magnetic fields.

III. PHENOMENA MEASURED TO OCCUR IN ASSOCIATION WITH RT IN-STABILITY AND RECONNECTION

Figures 3(a)-(d) are composites of the EUV (red) and visible light (blue) images captured by the double-branch imaging fiber bundle; the jet propagates toward the observer in these figures. The exposure and interframe times are 500 ns. As the jet kinks, the top of the spiral projection in this end-on view develops an RT instability and becomes bright in EUV (red) while the remainder dims in visible light (blue). The 5 cm $\times$ 3 cm bright EUV spot (red) is localized and lasts only ~ 1 μs. Since the visible light image is dark between the jet and the source electrode at 29.5-30.0 μs, the EUV-to-visible light ratio is extremely large.

Figures 4(a) and (b) are line-of-sight plasma emission spectra in the 347-353 nm range obtained respectively at 20-21 μs (i.e., before kink and RT instability) and at 28-30 μs
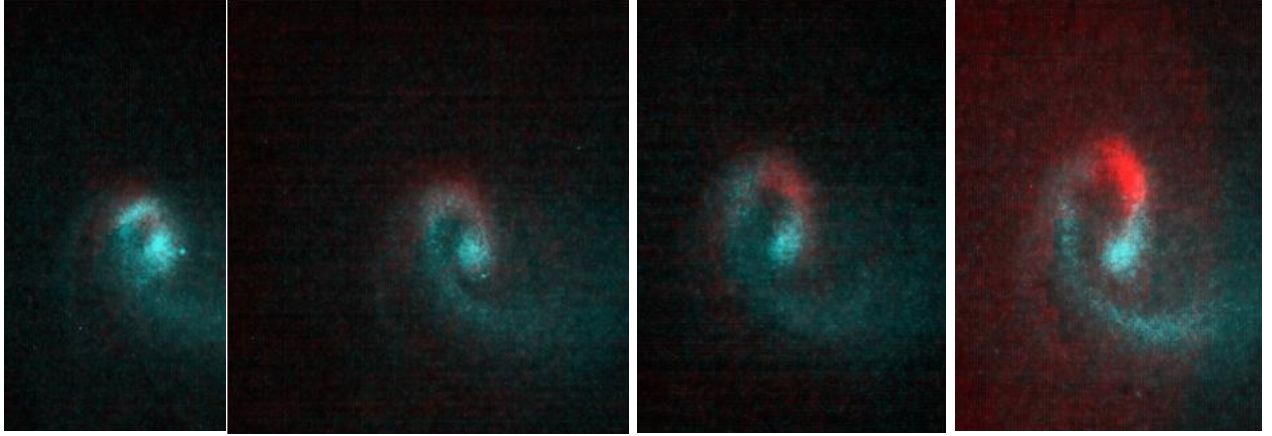
FIG. 3: Front view, composite EUV (red) and visible light (blue) images of the jet. As RT instability develops, the top part of the kinked jet becomes extremely bright in EUV but dims in visible light, indicating large T_e increase in top part.

(during RT instability). Figure 4(a) shows that both Ar II and Ar III lines exist before the kink while Fig. 4(b) shows disappearance of most Ar II lines (347.7, 349.2, 352.0, 352.1 nm) when the RT instability occurs and that only Ar III lines appear (348.1, 350.0, 350.4, 350.9, 351.1, 351.4 nm). This preponderance of Ar^{2+} ions relative to Ar^+ ions when RT instability occurs indicates T_e increases. It is also observed that a 303.8 nm Ar IV line exists at 28-30 μs but not at 20-21 μs providing further demonstration that RT instability increases T_e. The reconnection time is probably shorter than the ionization equilibration time but if LTE is nevertheless assumed, the Saha ionization equation indicates $T_e \simeq$ 5-10 eV in order to have 20-40 nm emission from Ar^{5+}-Ar^{7+} ions.

To obtain the ion temperature T_i and the electron density n_e, a Voigt function (convolution of Gaussian and Lorentzian functions) is fitted to the plasma emission spectra in Figs. 4(c) and (d). These spectra are respectively a 434.8 nm Ar II line obtained at 20-21 μs (i.e., before kink instability) and a 330.2 nm Ar III line obtained at 28-30 μs (i.e., during RT instability). This fitting gives both Doppler and Stark broadening allowing determination of T_i and n_e from a single spectral line [34]. Because asymmetries can provide as much as 25% error [34] spectral lines having high symmetry as well as high signal-to-noise ratio were selected. The Voigt analysis indicates $T_i = 2.6 \pm 0.4$ eV and $n_e = (1.6 \pm 0.3) \times 10^{22}$ m^{-3} at 20-21 μs while $T_i = 15.8 \pm 2.3$ eV and $n_e = (5.1 \pm 2.1) \times 10^{22}$ m^{-3} at 28-30 μs. This shows that ion heating also occurs during the RT instability and associated reconnection.
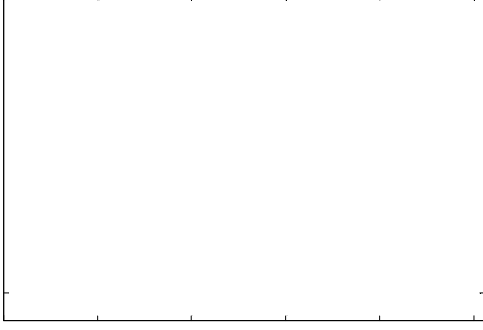
6

FIG. 4: Plasma emission spectra (a) at 20 μs (i.e., before kink instability) and (b) at 28 μs (i.e., start of RT instability). Almost all Ar II lines in (a) disappear in (b) indicating T_e increase. Plasma emission spectra (c) near 434.8 nm (Ar II) at 20 μs and (d) near 330.2 nm (Ar III) at 28 μs. Voigt fit of (c) and (d) gives Doppler broadening (w_D) and Stark broadening (w_S). Reconnection increases T_i and n_e from 2.8 eV and 1.4×10^{22} m^{-3} to 16.7 eV and 3.5×10^{22} m^{-3} respectively.

Figure 5(a), measurements obtained from the high frequency $\dot{B}$ probe, shows that strong broadband 3-D magnetic fluctuations occur in association with the RT instability and fast magnetic reconnection. Because the jet velocity is 10-20 km/s, jet motion across the 1 cm probe diameter produces up to 2 MHz convective magnetic fluctuations; these are removed by a digital highpass filter. The 100 MHz sampling rate of the data acquisition system resolves frequencies up to $\sim$20 MHz. Within the 2-20 MHz range, the $\dot{B}$ spectra have a $\sim \omega^{-1}$ power-law scaling as shown in Fig. 5(b). For a nominal $B = 0.6$ T magnetic field (assuming $I = 30$ kA and 1 cm jet radius), the singly ionized argon ion cyclotron frequency is $f_{ci} \sim 0.2$ MHz and the electron cyclotron frequency is $f_{ce} \sim 17$ GHz so the 2-20 MHz band is in the whistler regime.

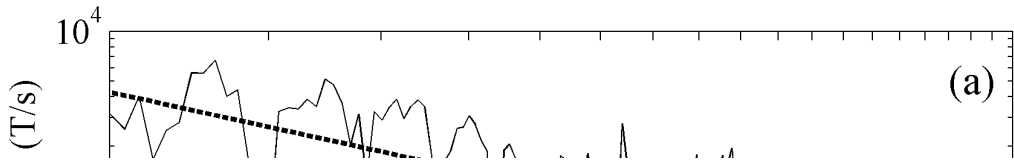The $\dot{B}_r$ spectrogram in Fig. 5(c) shows that low-frequency magnetic fluctuations start

FIG. 5: (a) $\dot{B}_r$ measured by probe having 150 T/s sensitivity. Inset from 26 to 31 μs shows magnetic fluctuations during RT instability. (b) $\dot{B}_r$ spectrum from 27 to 40 μs from fast Fourier transform. Linear regression shows this spectrum follows a $f^{-1.2}$ power-law; $\dot{B}_\phi, \dot{B}_z$ spectra are similar. (c) $\dot{B}_r$ spectrogram in time-frequency domain with color representing common logarithm of the amplitudes in T/s.
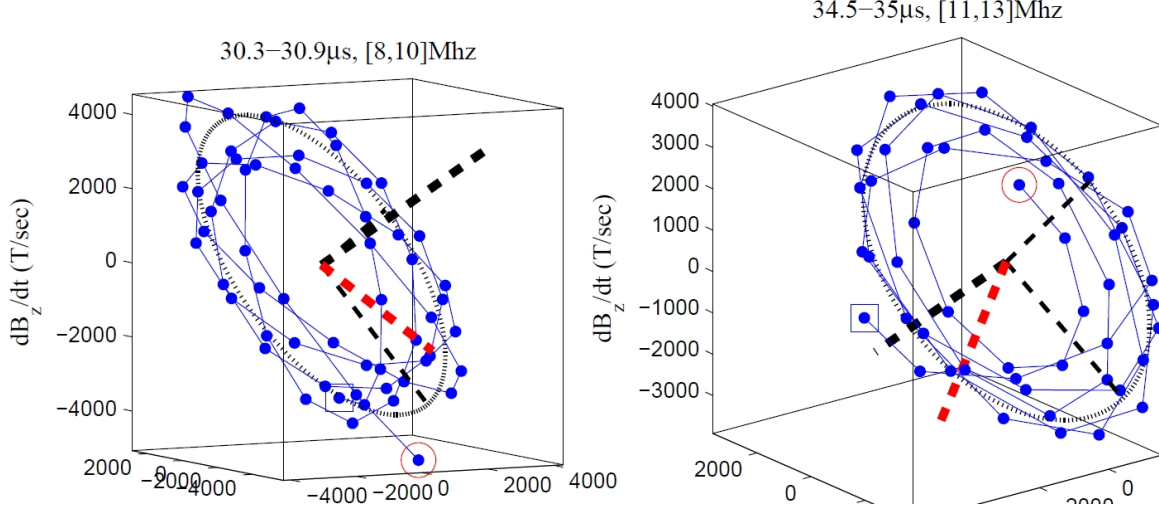
FIG. 6: (a) Hodogram of magnetic vector from 30.3 to 30.9 μs filtered by 8-10 MHz Butterworth digital filter. $\dot{B}_r, \dot{B}_\phi, \dot{B}_z$ are projected to a 2D plane selected by principle component analysis to obtain best-fitted ellipse (4.7×10^3 T/s major radius, 3.5×10^3 T/s minor radius). The blue square indicates the starting magnetic vector and the red circle indicates the ending magnetic vector. Thick black line shows normal to plane (wave vector direction) and is $(r, \phi, z) = (0.27, -0.82, 0.50)$ and is at angle 55° from the local magnetic field (thick red line). (b) Same as (a) except time range is 34.5 to 35.0 μs and frequency range is 11-13 MHz. Wave vector is $(r, \phi, z) = (-0.92, -0.39, -0.40)$ at 50° from local magnetic field $\mathbf{B}_0 = (-0.077T, -0.020T, -0.102T)$. Best-fit ellipse major/minor radii are 4.1×10^3 T/s and 3.2×10^3 T/s.

when the plasma jet reaches the probe ($\sim$15 μs) and then broadband high-frequency fluctuations appear when RT instability occurs ($\sim$30 μs). Figures 6(a) and (b), hodograms of the vector magnetic field in narrow frequency ranges, show that the magnetic fluctuations are circularly polarized; the angle between the wavevector and background magnetic field is typically < 60°. The observed magnetic field circular polarization of an obliquely propagating wave identifies the fluctuations to be whistler waves consistent with recent space observations [35] and recent models [36, 37].

Figure 7(a) shows the time-dependence of the voltage across the electrodes and Fig. 7(b) shows the electric current. The plasma ignites with application of 5 kV which drops to 2 kV immediately after breakdown. The electric current peaks at 110 kA at 7-8 μs and remains

FIG. 7: (a) Voltage across the electrodes showing spikes when RT instability and bright EUV spot occur. (b) Current flowing through electrodes.

at 50-60 kA until 50 μs. At 30 μs distinct, reproducible > 500 volt spikes (indicated by the arrow) lasting ~ 1 μs appear across the electrodes; this is when the RT instability occurs and the EUV becomes bright. These voltage spikes seem to result from magnetic reconnection that changes the magnetic flux linking the electrode circuit. Voltage spikes sometimes also appear at other times and presumably result from rapid flux changes at other locations. For example, Fig. 7(a) also contains a voltage spike at 25 μs but, unlike the RT-associated spikes at $\sim$30 μs, this spike and others not at times of RT instability are not reproducible from shot to shot.

IV. DISCUSSION

A. Magnetic field profile

Our plasma jet involves three progressively smaller scales: (i) axisymmetric jet before kinking, (ii) kinking, and (iii) RT instability. Scale (i) has been imaged, measured with a movable 60-coil magnetic probe array (20 clusters of 3 orthogonal coils, clusters having 2 cm spacing), and modeled using a numerical MHD code which gives magnetic fields in good

10

agreement with the field measured by the magnetic probe array (see Figs. 4, 10, and 11 in Ref. [38]). This agreement is consistent with the MHD concept that magnetic field is frozen into the plasma and indicates that the images show the magnetic field configuration. Thus, at this scale the images constitute 'seeing' how the magnetic field evolves.

Scale (ii), the kinking, shows images that are in excellent agreement with the predictions of free-boundary MHD instability theory [25]. This theory predicts that the magnetic field will develop an exponentially growing helical shape and since MHD predicts plasma is frozen to the magnetic field, it predicts the plasma should have an exponentially growing helical shape. This is what is observed and so one can conclude that at this scale, the images also constitute 'seeing' how the magnetic field evolves.

Scale (iii), the RT instability has a length scale too small to be resolved by the magnetic probe array. The structure becomes very complicated but the existence of the ripples is very reproducible as seen in Figs. 2(a) and (b) which are photos of two different shots having identical experimental settings. These photos show that because the kink is rotating around, the actual physical location of the rippled jet in three-dimensional space differs from shot to shot. The theoretical calculation which is constructed from a numerical evaluation of an analytic mode-coupling calculation for the early phase of the RT instability [32, 33] reveals that the calculated ripples are such that the ripples exist on the trailing side of the kink-accelerated jet and that at this trailing side $\mathbf{k} \cdot \mathbf{B}$ is near-zero where $\mathbf{k}$ is the ripple wavevector and $\mathbf{B} = B_z \hat{z} + B_\theta \hat{\theta}$ is the local 'equilibrium' magnetic field, i.e., the helical magnetic field of the kinked jet at the trailing side. This is consistent with the slab-geometry result that the fastest growing Rayleigh-Taylor instability has $\mathbf{k} \cdot \mathbf{B} = 0$ so that field lines are interchanged without changing the magnetic energy [39, 40].

The ripples grow exponentially and when they become large, drastically affect the flux tube so that the topology of the magnetic field and the current will have to change, i.e., there will be a magnetic reconnection. Due to the temporal and spatial limitations of the resolution of the diagnostics, the exact 3-D topology of the complex magnetic reconnection is unclear. However, the magnetic reconnection is presumably located where the EUV images get extremely bright (see Fig. 3).

B. Electron ohmic heating and ion stochastic heating

The calculated electron Ohmic heating rate is $6.4 \times 10^9 < \eta J^2 < 1.3 \times 10^{13}$ Wm^{-3} using Spitzer resistivity [41] $\eta = 1.03 \times 10^{-4} T_e^{-3/2} Z \ln \Lambda$ Ω m $= 3.3 \times 10^{-5}$ Ω m with $T_e = 10$ eV. The wide range of the calculated Ohmic heating rate results from uncertainty in the current channel size and the fraction of total current in the current channel. The observed electron heating rate $4.2 \times 10^{10} < 3n_e \Delta(k_B T_e)/2\Delta t < 1.8 \times 10^{11}$ Wm^{-3} is within the range of the calculated electron Ohmic heating rate so Ohmic heating is a plausible electron heating mechanism.

The ion Ohmic heating rate is smaller than the electron Ohmic heating rate by $m_e/m_i \simeq 10^{-5}$, so Ohmic dissipation cannot explain the rapid observed ion heating from 2.6 eV to 16 eV shown in Figs. 4(c) and (d). The electron-ion energy transfer rate ($5 \times 10^5 < \nu_{Eei} < 1.2 \times 10^6$ s^{-1} for $T_e = 10$ eV) could marginally explain T_i reaching 10 eV if n_e is at its maximum but could not explain the observed T_i exceeding T_e. Stochastic ion heating [42–45] is a likely candidate to explain such a strong ion heating. This heating mechanism occurs when a radially-dependent electrostatic potential fluctuation satisfies the stochasticity threshold condition

$$\frac{m_i}{q_i B^2} \left| \frac{\partial^2 \tilde{\phi}}{\partial r^2} \right| > 1. \tag{1}$$

This condition can also be seen by considering the Lorentz equation for a parabolic repulsive electrostatic potential so $m\dot{\mathbf{v}} = q(E_0 \mathbf{r}/a + \mathbf{v} \times \mathbf{B})$; if $\mathbf{r} \sim \mathbf{r}_0 \exp(i\omega t)$ is assumed, then $\omega = \left(-\omega_c \pm \sqrt{\omega_c^2 - 4qE_0/(ma)}\right)/2$ [46, 47] which implies exponentially growing $\mathbf{r}$ and $\mathbf{v}$ if $4qE_0/(ma\omega_c^2) > 1$.

The 3-D reconnection process can be considered as involving a local rapid change of field-aligned current (see Fig. 1c of Ref [48] for the detailed coordinate system), i.e., $J_z \simeq J_{z0}e^{-t/\tau}$ where $\tau \sim$ reconnection time scale (z direction here is not the axial direction of the experiment but the direction of the local guide magnetic field). Ampere's law shows $B_\theta = \mu_0 J_{z0} r e^{-t/\tau}/2$ corresponding to $A_z(r, z, t) = -\int_0^r dr B_\theta = -\mu_0 J_{z0} r^2 e^{-t/\tau}/4$. The generalized Ohm's law with finite electron inertia included is

$$\mathbf{E} + \mathbf{U} \times \mathbf{B} - \frac{1}{ne}\mathbf{J} \times \mathbf{B} = \eta \mathbf{J} + \frac{c^2}{\omega_{pe}^2}\mu_0 \frac{\partial \mathbf{J}}{\partial t}. \tag{2}$$

Using $\mathbf{B} = B_z \hat{z} + B_\theta \hat{\theta}$, $\mathbf{J} = J_z \hat{z}$ and $\mathbf{E} = -\nabla \phi - \partial \mathbf{A}/\partial t$ the z component of the generalized

Ohm's law is

$$-\frac{\partial \phi}{\partial z} - \frac{\partial A_z}{\partial t} + \hat{z} \cdot \mathbf{U}_T \times \mathbf{B}_T - \frac{1}{ne}\hat{z} \cdot \mathbf{J}_T \times \mathbf{B}_T = \eta J_z + \frac{c^2}{\omega_{pe}^2}\mu_0 \frac{\partial J_z}{\partial t} \tag{3}$$

where the subscript T denotes components transverse to z. In two-dimensional analyses of magnetic reconnection, $\partial/\partial z = 0$ so there would be no electrostatic term $\partial\phi/\partial z$ but here the reconnection is localized in three dimensions so $\partial/\partial z \neq 0$. Localization in three dimensions means that U_r and B_r are finite at some specific axial location which will be denoted $z = 0$ but go to zero at axial locations outside this reconnection region. The Hall term is important at radii smaller than the ion skin depth c/ω_{pi} and the electron inertia term (last term on RHS of Eq. 2) becomes important at radii of the order of the even smaller electron skin depth scale c/ω_{pe}. We assume that Hall reconnection is important but consider a region axially and radially just outside the reconnection region so in this external region the Hall term and the electron skin depth term are relatively small compared to the other terms and so can be neglected. Because this external region is axially displaced from $z = 0$ (i.e. from where $\hat{z} \cdot \mathbf{U}_T \times \mathbf{B}_T = U_r B_\theta - U_\theta B_r$ is finite) $\hat{z} \cdot \mathbf{U}_T \times \mathbf{B}_T$ can also be neglected and so this external region is effectively governed by resistive MHD in contrast to the internal region which is governed by Hall MHD. This external region then would be slightly larger than c/ω_{pi} but not enormously larger as the the relation between inner and outer regions of magnetic reconnection is such that the outer scale of the inner region corresponds to the inner scale of the outer region. Thus, with these assumptions Eq. 3 in the external region (i.e., slightly larger than c/ω_{pi} region) reduces to

$$-\frac{\partial \phi}{\partial z} - \frac{\partial A_z}{\partial t} \simeq \eta J_z \tag{4}$$

which is just the parallel Ohm's law when the Hall and electron inertia terms are not important and $U_r = 0$, $B_r = 0$. Equation 4 can be integrated with respect to z to give

$$\phi(r, z, t) \simeq -\int_0^z \left(\frac{\partial A_z}{\partial t} + \eta J_z\right) dz. \tag{5}$$

Since J_z is independent of r while A_z depends on r this gives

$$\frac{\partial^2 \phi}{\partial r^2} \simeq -\frac{\partial^2}{\partial r^2}\int_0^z \frac{\partial A_z}{\partial t} dz \simeq -\frac{1}{2\tau}\mu_0 J_{z0} z e^{-t/\tau} \tag{6}$$

so using Eq. 1 ion orbits will be stochastic (exponentially growing) if $\tau < m_i(q_i B^2)^{-1}\mu_0 J_{z0} z$. Using nominal $z = 2$ cm, $B_z = 0.6$ T, and $J_{z0} = 10^8$ A m^{-2} predicts Ar ion orbits will be stochastic if $\tau < 3$ μs.

In order to confirm the possibility of stochastic heating the separation distance between two adjacent ions assuming $\tau = 1$ μs and $\tau = 100$ μs was calculated by numerically integrating the Lorentz equations with the above electric and magnetic fields. Figures 8(a) and (b) show the calculated results; note the different vertical axis scales in Figs. 8(a) and (b). Here, we assumed ions do not collide with other ions. As predicted, the separation distance grows exponentially for $\tau = 1$ μs but not for $\tau = 100$ μs. Since the experimentally observed reconnection has a time scale of order 1 μs, the ions are clearly in the stochastic regime and will have stochastic trajectories (i.e., exponentially increasing inter-ion separation corresponding to rapidly increasing random velocities). The ions are effectively falling off the potential hill associated with the potential $\phi \sim -r^2$ because the magnetic field is too weak for the ions to undergo $\mathbf{E} \times \mathbf{B}$ drifts. Ion-ion collisions do not inhibit this falling off the potential hill, i.e., collisions do not inhibit stochastic heating mechanism but only provide additional randomization so this stochastic ion heating could occur even though the 1-10 ns ion-ion collision time is much smaller than τ.

The effect of collisions is further investigated by including pseudo-collisions in the numerical integration of Lorentz equations as follows: we generate 1000 particles in the first quadrant ($x > 0$, $y > 0$); the initial positions are randomly chosen. Ions are assumed to have an initial random thermal motion equivalent to 2 eV and then each ion collides with randomly chosen ions every 5 ns. Ions exchange their momentum and energy via elastic collisions with a random contact angle but the position of the colliding ions is set to be unchanged after the collision. The calculated energy distributions of 1000 ions at 1 μs for $\tau = 1$ μs and for $\tau = 100$ μs are respectively displayed in Figs. 8(c) and (d) and show that the ions quickly gain kinetic energy when the stochastic threshold is breached. Note the different horizontal axis scales in Figs. 8(c) and (d).

C. Hall-MHD reconnection and whistler waves

We believe Hall-MHD reconnection is likely to occur in our plasma because i) the reconnection process depends on Hall term physics [16, 21] when the current channel becomes constricted to similar to c/ω_{pi} and the jet diameter is observed to be of the same order of magnitude as the ion skin depth when the RT instability occurs, ii) whistler waves, a Hall-MHD phenomenon, are observed when the jet breaks from its source electrode in association
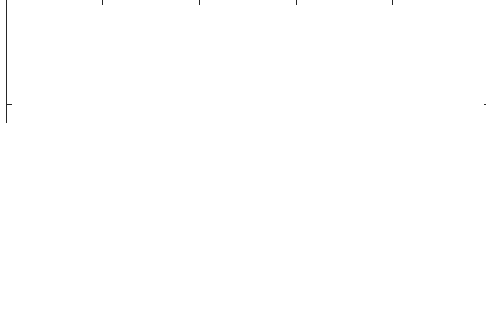
FIG. 8: Differences between the positions of two initially adjacent particles, $\delta\mathbf{x} = \mathbf{x}_1 - \mathbf{x}_2$, obtained by numerical integration of the Lorentz equations (a) with $\tau = 1$ μs and (b) with $\tau = 100$ μs. Note the different vertical scales for the two plots. Kinetic energy distribution at 1 μs (c) with $\tau = 1$ μs and (d) with $\tau = 100$ μs.

with the RT instability, and iii) using the nominal value of $B = 0.6$ T and the measured values of $n = 1.6 \times 10^{22}$ m^{-3} and $T_e = 2.6$ eV, the Hall term $(\mathbf{J} \times \mathbf{B}/ne)$ and resistive term $(\eta\mathbf{J})$ are calculated to have the same order of magnitude in the generalized Ohm's law. An alternative scenario is that resistive MHD reconnection occurs first and the whistler waves are kinetically destabilized by anisotropic electron heating associated with reconnection; this alternative scenario is considerably more complicated and so seems less likely.

On including electron-ion collisions by making the replacement $m_e \rightarrow m_e(1 + i\nu_{ei}/\omega)$, the whistler dispersion [49] becomes $\omega = (|\omega_{ce}| k_\parallel/k - \omega - i\nu_{ei})k^2c^2/\omega_{pe}^2$; assuming $B \simeq 0.6$ T and $k_\parallel/k \simeq 0.5$ shows whistlers propagate undamped if $\nu_{ei} < 5 \times 10^{10}$ s^{-1}. It is seen that $\nu_{ei} = 1.5 \times 10^{11}$ s^{-1} for $T_e = 2.6$ eV and $n = 1.6 \times 10^{22}$ m^{-3} (before RT instability) and $\nu_{ei} = 6.5 \times 10^{10}$ s^{-1} for $T_e = 10$ eV and $n = 5.1 \times 10^{22}$ m^{-3} (after RT instability) so

the propagation of whistler waves through the main jet region could be damped. However, the plasma density between the reconnection region and the location where whistler waves were measured is much lower than that of the main jet region and thus the propagation of whistler waves is undamped as whistler waves escape the main jet region.

Ji et al. [19] previously reported MRX observations showing whistler waves to be associated with magnetic reconnection. However, unlike the MRX experiments where the reconnection was driven by modulating coil currents and was two-dimensional, here the reconnection is localized in three dimensions and is spontaneous as it results from a kink-induced RT instability. Also, the reconnection region density here is four orders of magnitude larger than in MRX so that the electron mean free path ($\sim 10\ \mu$m) is much smaller than the current channel size (~ 1 cm). The observation that kink-induced RT instability causes fast reconnection involving Hall-whistler physics suggests that Hall physics likely underlies Taylor relaxation in spheromak and RFP plasmas.

V.   CONCLUSION

When the Rayleigh-Taylor instability induced by a kink instability pinches the radius of a plasma jet to be similar to the ion skin depth, it is observed that the following phenomena occur: i) a drastic change in plasma topology, ii) a strong EUV burst indicating localized electron heating, iii) Doppler broadening in plasma emission spectra indicating fast ion heating, iv) obliquely propagating, right-handed circularly polarized whistler waves, and v) a strong, transient voltage spike indicating a sudden change in magnetic flux. These observations are presumed to correspond to a Hall-MHD magnetic reconnection. We showed that the observed electron heating is likely caused by the Ohmic dissipation and the ion heating plausibly results from the stochastic ion trajectories associated with a rapidly changing field-aligned current. The generation mechanism of whistler waves is not well understood yet and will be studied in the future.

[1] X. H. Deng and H. Matsumoto, Nature **410**, 557 (2001).

[2] F. S. Mozer, S. D. Bale, and T. D. Phan, Physical Review Letters **89**, 015002 (2002).

[3] K. Shibata and T. Magara, Living Reviews in Solar Physics **8**, 6 (2011).

[4] J. A. Wesson, Nuclear Fusion **30**, 2545 (1990).

[5] J. B. Taylor, Physical Review Letters **33**, 1139 (1974).

[6] T. R. Jarboe, Plasma Physics and Controlled Fusion **36**, 945 (1994).

[7] H. A. B. Bodin and A. A. Newton, Nuclear Fusion **20**, 1255 (1980).

[8] R. N. Dexter, D. W. Kerst, T. W. Lovell, S. C. Prager, and J. C. Sprott, Fusion Technology **19**, 131 (1991).

[9] E. N. Parker, Journal of Geophys. Research **62**, 509 (1957).

[10] P. A. Sweet, in *Electromagnetic Phenomena in Cosmical Physics*, edited by B. Lehnert (Cambridge University Press, 1958).

[11] L. Golub, J. Bookbinder, E. DeLuca, M. Karovska, H. Warren, C. J. Schrijver, R. Shine, T. Tarbell, A. Title, J. Wolfson, et al., Physics of Plasmas **6**, 2205 (1999).

[12] D. Biskamp, E. Schwarz, and J. F. Drake, Physics of Plasmas **4**, 1002 (1997).

[13] J. Birn, J. F. Drake, M. A. Shay, B. N. Rogers, R. E. Denton, M. Hesse, M. Kuznetsova, Z. W. Ma, A. Bhattacharjee, A. Otto, et al., Journal of Geophysical Research-Space Physics **106**, 3715 (2001).

[14] J. F. Drake, M. A. Shay, and M. Swisdak, Physics of Plasmas **15**, 042306 (2008).

[15] K. Fujimoto and R. D. Sydora, Geophysical Research Letters **35**, Art. No. L19112 (2008).

[16] P. M. Bellan, Physics of Plasmas **21**, 102108 (2014).

[17] W. Gekelman and R. L. Stenzel, Journal of Geophysical Research-Space Physics **89**, 2715 (1984).

[18] M. Oieroset, T. D. Phan, M. Fujimoto, R. P. Lin, and R. P. Lepping, Nature **412**, 414 (2001).

[19] H. T. Ji, S. Terry, M. Yamada, R. Kulsrud, A. Kuritsyn, and Y. Ren, Physical Review Letters **92**, 115001 (2004).

[20] P. Petkaki, M. P. Freeman, and A. P. Walsh, Geophysical Research Letters **33** (2006).

[21] N. Attico, F. Califano, and F. Pegoraro, Physics of Plasmas **7**, 2381 (2000).

[22] J. Yoo, M. Yamada, H. T. Ji, J. Jara-Almonte, and C. E. Myers, Physics of Plasmas **21**, 055706 (2014).

[23] Y. Ono, H. Tanabe, Y. Hayashi, T. Ii, Y. Narushima, T. Yamada, M. Inomoto, and C. Z. Cheng, Physical Review Letters **107**, 185001 (2011).

[24] S. You, G. S. Yun, and P. M. Bellan, Physical Review Letters **95**, 045002 (2005).

[25] S. C. Hsu and P. M. Bellan, Physical Review Letters **90**, 215002 (2003).

[26] A. L. Moser and P. M. Bellan, Nature **482**, 379 (2012).

[27] E. B. Hooper, T. A. Kopriva, B. I. Cohen, D. N. Hill, H. S. McLean, R. D. Wood, S. Woodruff, and C. R. Sovinec, Physics of Plasmas **12**, 092503 (2005).

[28] K. B. Chai and P. M. Bellan, Review of Scientific Instruments **84**, 123504 (2013).

[29] G. S. Yun and P. M. Bellan, Physics of Plasmas **17**, 062108 (2010).

[30] C. Carobbi, L. Millanta, and L. Chiosi, in *Electromagnetic Compatibility, 2000. IEEE International Symposium on* (2000), vol. 1, pp. 35–40.

[31] R. J. Perkins and P. M. Bellan, Radio Frequency Power in Plasmas: Proceedings of the 19th Topical Conference **1406**, 19th Topical Conference on Radio Frequency Power in Plasmas/US (2011).

[32] X. Zhai and P. M. Bellan, Physics of Plasmas **xx**, submitted (2015).

[33] X. Zhai, Ph.D. thesis, California Institute of Technology (2015).

[34] G. V. Vogman and U. Shumlak, Review of Scientific Instruments **82**, 103504 (2011).

[35] B. T. Tsurutani, O. P. Verkhoglyadova, G. S. Lakhina, and S. Yagitani, Journal of Geophysical Research-Space Physics **114**, A03207 (2009).

[36] O. P. Verkhoglyadova, B. T. Tsurutani, and G. S. Lakhina, Journal of Geophysical Research-Space Physics **115**, Art. No. A00F19 (2010).

[37] P. M. Bellan, Phys. Plasmas **20**, 082113 (2013).

[38] X. Zhai, H. Li, P. M. Bellan, and S. T. Li, Astrophysical Journal **791**, 40 (2014).

[39] S. Chandrasekhar, *Hydrodynamic and Hydromagnetic Stability* (Clarendon, Oxford, 1961), eq.234, p.466.

[40] G. Bateman, *MHD Instabilities* (MIT Press, Cambridge, Mass., 1978), p.56.

[41] L. Spitzer, *Physics of fully ionized gases; 1st ed.* (Interscience, New York, NY, 1956).

[42] J. M. McChesney, R. A. Stern, and P. M. Bellan, Physical Review Letters **59**, 1436 (1987).

[43] K. Stasiewicz, R. Lundin, and G. Marklund, Physica Scripta **T84**, 60 (2000).

[44] J. Vranjes and S. Poedts, Monthly Notices of the Royal Astronomical Society **408**, 1835 (2010).

[45] K. Stasiewicz, S. Markidis, B. Eliasson, M. Strumik, and M. Yamauchi, Epl **102**, 49001 (2013).

[46] R. C. Davidson, *Theory of Nonneutral Plasmas* (W. A. Benjamin, Reading, MA, 1974), see Eq.1.2.9.

[47] P. M. Bellan, Journal of of Plasma Physics **82**, Art. No. 615820101 (2016).

[48] P. M. Bellan, Physics of Plasmas **5**, 3081 (1998).

[49] T. H. Stix, *Waves in Plasmas* (American Institute of Physics Press, New York, 1992).